Supplementary Information (SI) for Energy & Environmental Science.

Supporting Information

All-organic siloxane strengthening polymer dielectric for high-temperature capacitive energy storage at harsh-environment electronics

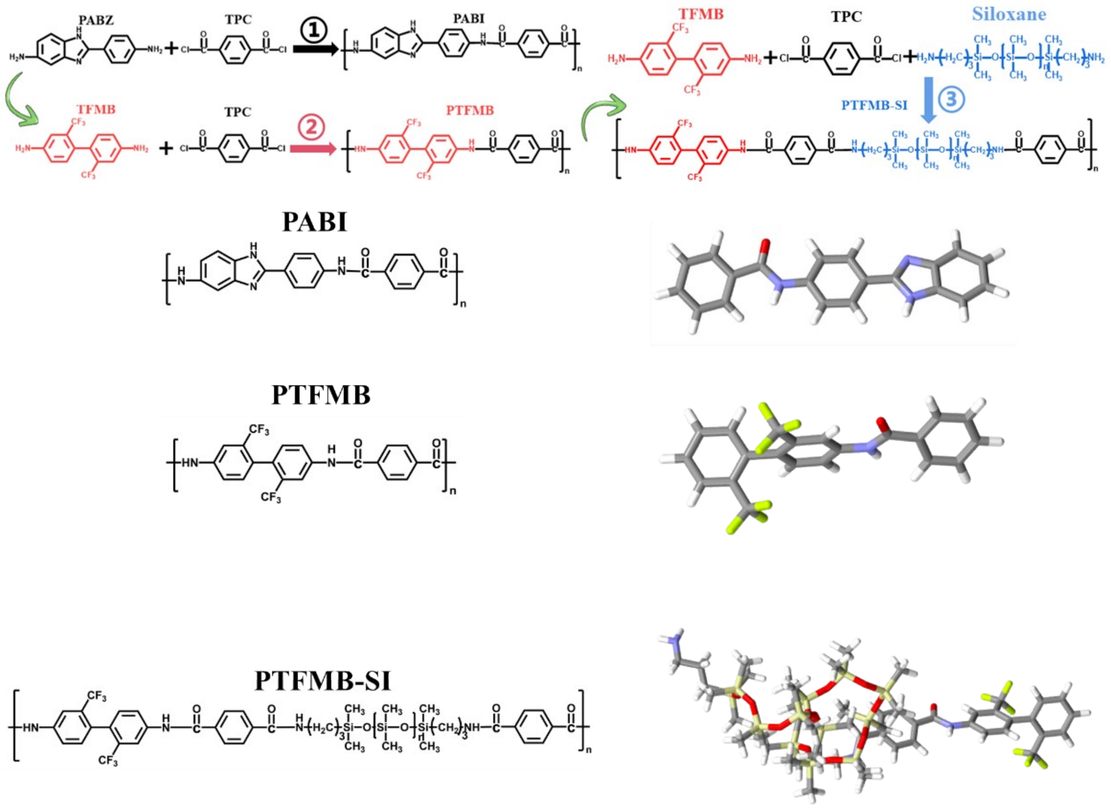

Figure S1. Synthetic processes, chemical structures and molecular models of different polyamide films.

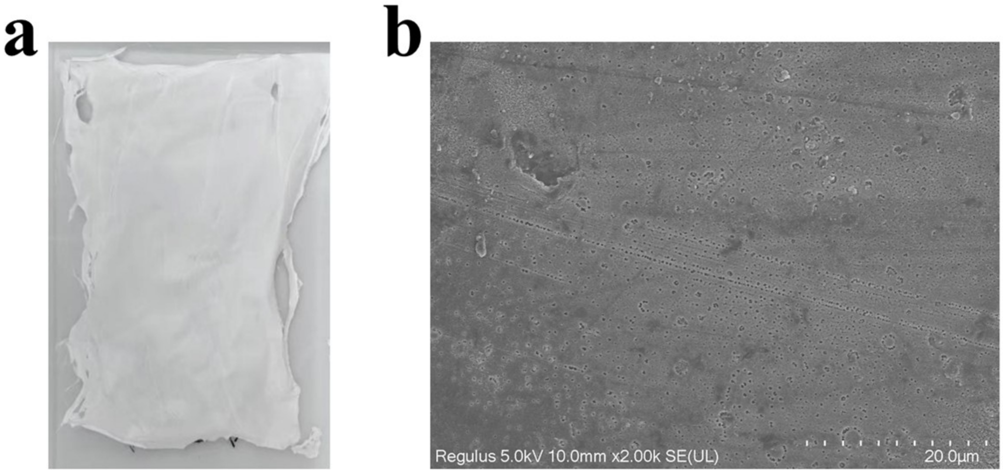

Figure S2. Photo and SEM images of PTFMB-15%SI film at the siloxane content up to 15%.

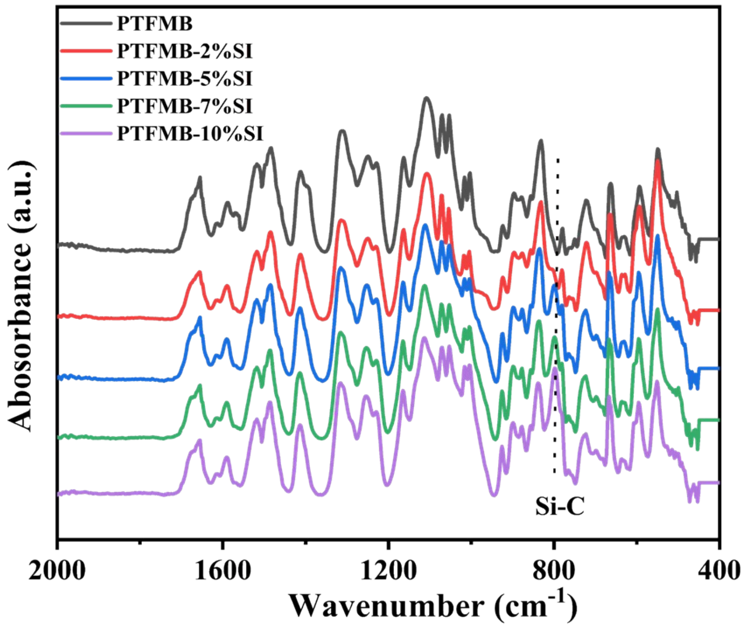

Figure S3. ATR-FTIR spectra of siloxane modified PTFMB films.

The infrared spectra of siloxane modified PTFMB indicated that with increasing siloxane content, the absorption peak of the Si-C bond at 800 cm^{-1} gradually intensifies. The results showed that the siloxane was successfully introduced into the molecular structure of PTFMB by copolymerization.

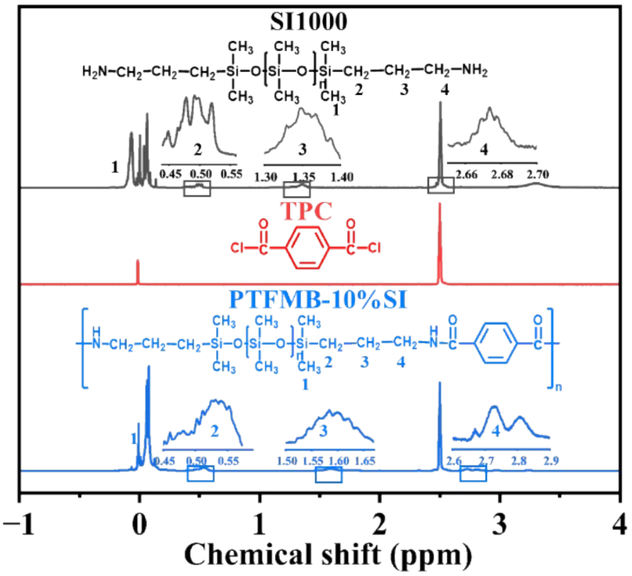

Figure S4-1. Comparison of NMR spectra of siloxane unit (SI1000), TPC and PTFMB-10%SI.

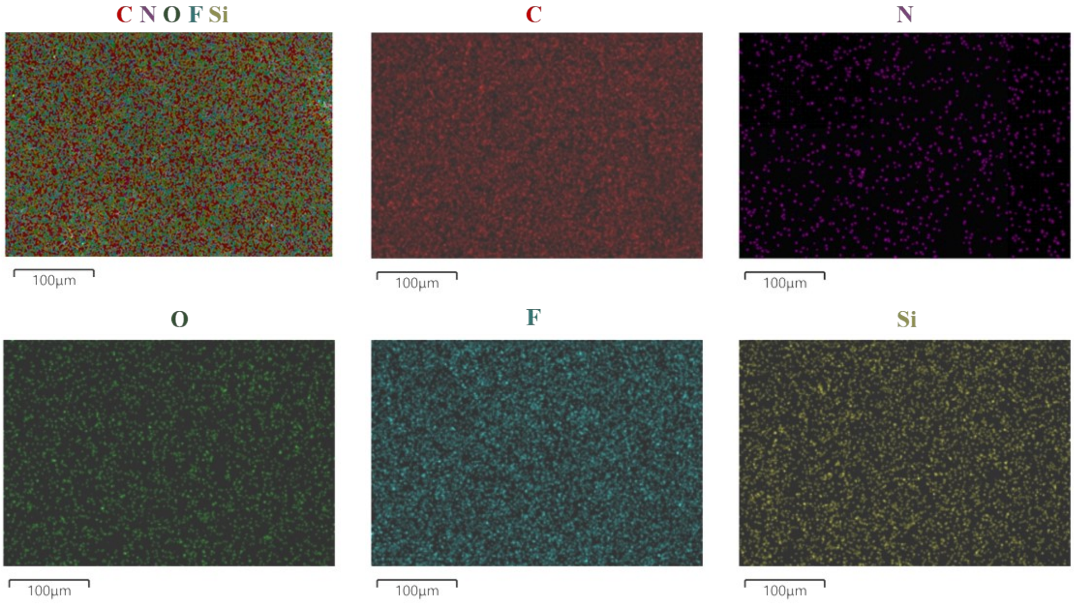

Figure S4-2. Corresponding EDS mapping of C, N, O, F, and Si elements of PTFMB-10%SI film.

The EDS spectra of the PTFMB-10%SI film demonstrate the uniform distribution of C, N, O, F, and Si elements within the film. This result indicates successful incorporation of siloxane unit into the PTFMB matrix, achieving their uniform dispersion within the matrix.

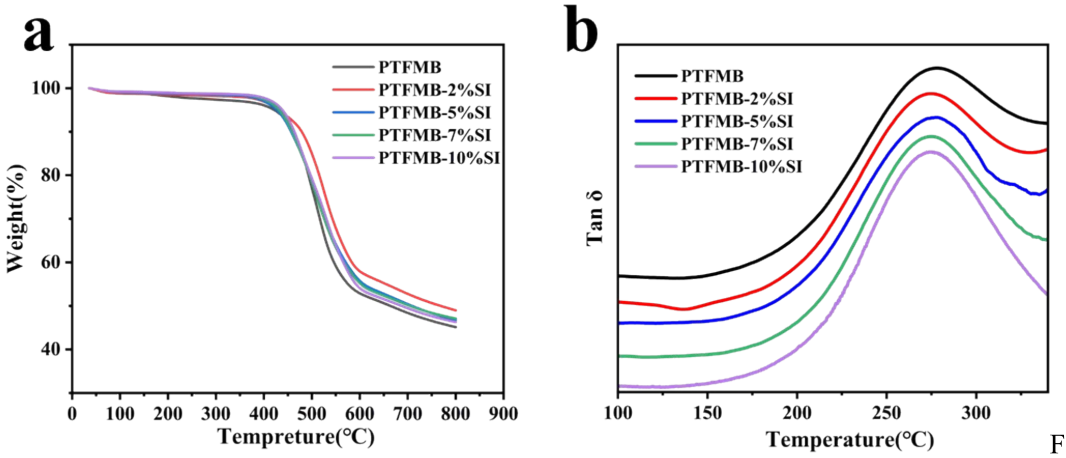

Figure S5. TGA and DMA curves of siloxane modified PTFMB films.

Table S1. Heat-resistant properties of siloxane modified PTFMB films.

Sample	PTFMB	PTFMB-2%SI	PTFMB-5%SI	PTFMB-7%SI	PTFMB-10%SI
T_5	421	431	426	431	438
T_{10}	462	478	456	458	463
T_g	278	276	275	274	274

T_5 : Temperature at which 5% weight loss was recorded by TGA.

T_{10} : Temperature at which 10% weight loss was recorded by TGA.

T_g : Measured by DMA .

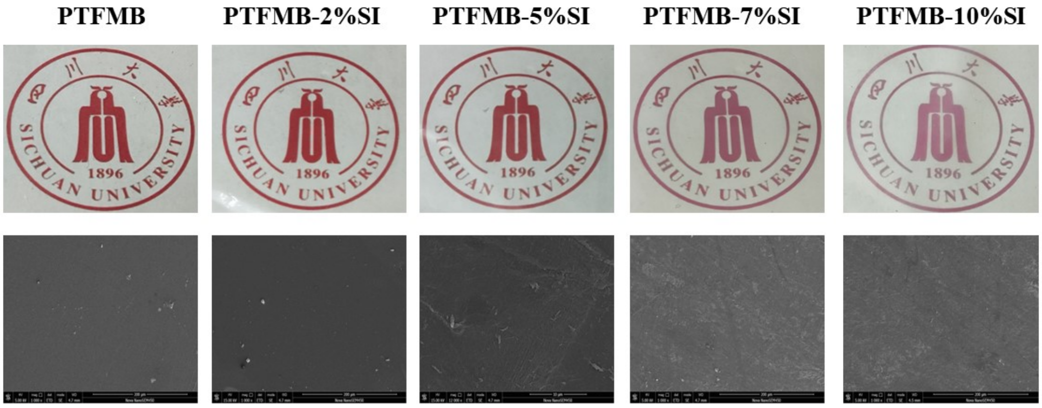

PTFMB **PTFMB-2%SI** **PTFMB-5%SI** **PTFMB-7%SI** **PTFMB-10%SI**

Figure S6. Photograph and SEM images of siloxane modified PTFMB films.

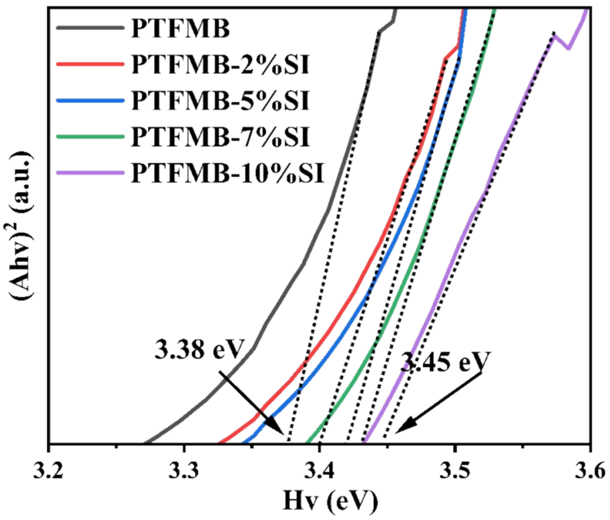

Figure S7. Calculated E_g based on UV-Vis results of siloxane modified PTFMB films.

With the siloxane content increasing, the optical bandgap (E_g) of the siloxane modified PTFMB film also increases. Upon adding 10% siloxane unit, the optical bandgap of PTFMB-10%SI rises from 3.38 eV to 3.45 eV.

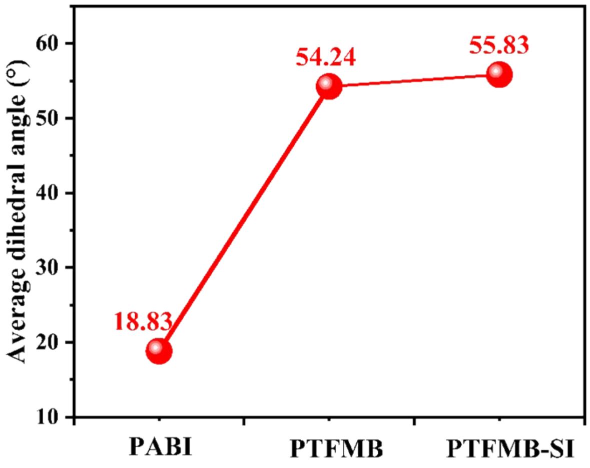

Figure S8. Average dihedral angles of PABI, PTFMB and PTFMB-SI.

By examining the dihedral angles between adjacent benzene rings in PABI, PTFMB and PTFMB-SI model molecules under conditions of minimum energy, it is observed that PTFMB exhibits a twisted conformation, resulting in larger dihedral angles. Introduction of siloxane unit further increases the dihedral angle between adjacent benzene rings, thereby suppressing π-π stacking and intermolecular charge transfer complex (CTC) formation. This effectively impedes charge carrier transport between the chains.

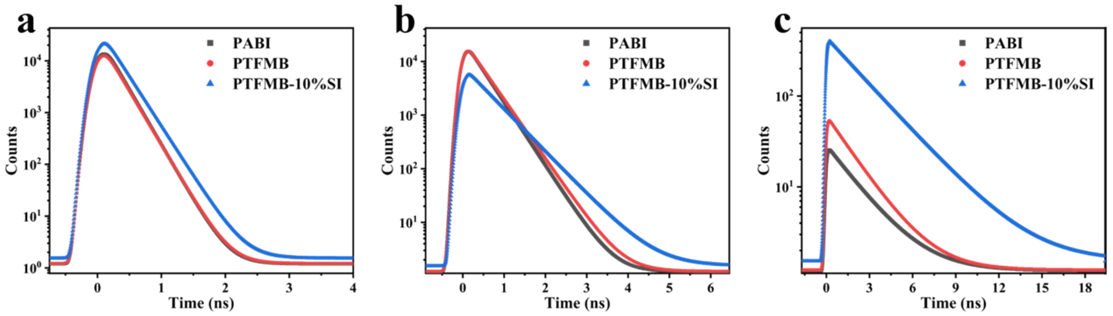

Figure S9. Positron annihilation lifetime spectra of PABI, PTFMB and PTFMB-10%SI films for the analysis of different lifetime components of τ_1, τ_2, and τ_3, respectively.

Table S2. Summary of analyzed PALS data for PABI, PTFMB and PTFMB-10%SI films.

Materials	τ_1(ns)	τ_2(ns)	τ_3(ns)	I_1(%)	I_2(%)	I_3(%)	R(Å)	V_{PALS}(Å^3)
PABI	0.20	0.39	1.84	35.51	63.75	0.72	2.7	82.9
PTFMB	0.20	0.36	2.06	38.49	61.12	0.37	2.9	103.3
PTFMB-10%SI	0.22	0.54	2.52	63.51	29.14	7.33	3.3	148.6

The results reveal three distinct exponential decay components (τ_1, τ_2, and τ_3). The first lifetime component (τ_1) corresponds to the lifetime of positrons in para-positronium (p-Ps). The second lifetime component (τ_2) is attributed to the free annihilation lifetime of positrons. The longest lifetime component (τ_3) is associated with ortho-positronium (o-Ps) annihilation, and it uniquely provides information about the size and quantity of nanoscale voids in these materials. PTFMB-10%SI exhibits the longest τ_3 lifetime and the highest proportion of τ_3, indicating that it has the largest free volume fraction within the confined space. This is favorable for the rotational motion of dipoles, reducing frictional losses.

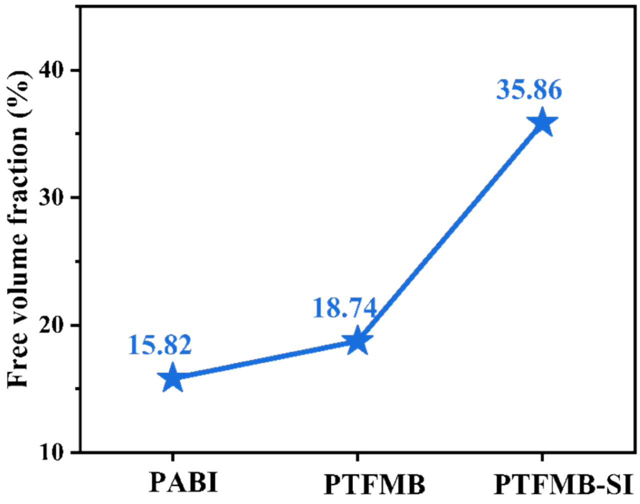

Figure S10. Free volume fraction of PABI, PTFMB and PTFMB-SI.

Comparative analyses reveal the densely packed nature of PABI chains (free volume fraction: 15.82%). In the case of PTFMB, which is characterized by substantial steric hindrance, there is a marginal increase in the free volume fraction to 18.74%. In sharp contrast, the twisted structure of siloxane-containing segments in PTFMB-SI, distinguished by low interaction force and a high curl degree, interferes with chain stacking and enhances void space. This results in a remarkable free volume fraction increase up to 35.86%. The increased free volume provides ample rotational space for dipoles, effectively reducing polarization losses.

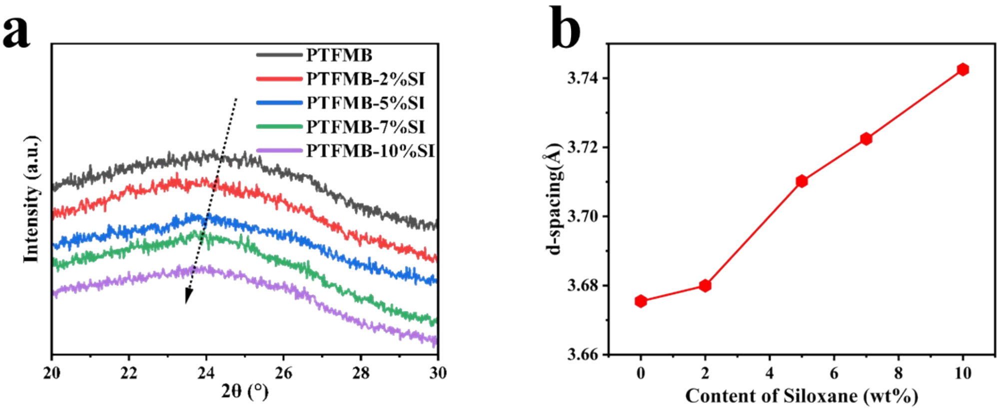

Figure S11. (a) XRD diffraction profiles of siloxane modified PTFMB films. (b) Interchain spacing of siloxane modified PTFMB films calculated from the X-ray profiles' peak positions.

Analysis of peak positions in X-ray diffraction spectra allows the calculation of intermolecular chain distance for different samples. The increased siloxane content gradually increases the intermolecular chain distance (d) of PTFMB-SI from 3.68 Å to 3.74 Å.

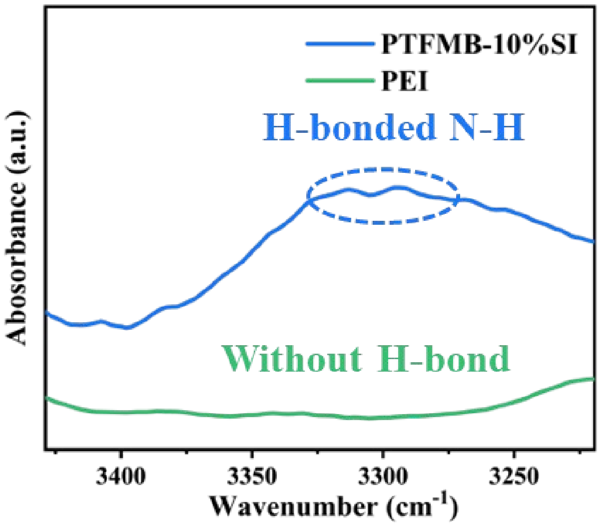

Figure S12. ATR-FTIR spectra of PEI and PTFMB-10%SI films.

PTFMB-10%SI has an obvious N-H absorption peak near 3330 cm^{-1} that reflects the formation of strong hydrogen bonds, while PEI does not find such an absorption peak here. This result proves that the strong hydrogen bonds are existed in PTFMB-10%SI, which is capable of providing the excellent mechanical properties.

Table S3. Comparisons of mechanical strength and Young's Modulus between this work and other reported dielectric polymers.

Sample	Strength (MPa)	Young's Modulus (GPa)
BOPP	115	3.5
PET	202	4.3
PEI[1]	80	2.8
PEEK[2]	97	3.6
PI-NH_2-POSS[1]	95	1.8
PEI-O-AOC[3]	139	2.9
PTFMB-10%SI (this work)	321	9.8

Notably, the currently reported polymer dielectrics in literature exist an intractable and contradictory problem of synergistically enhancing the mechanical strength and energy storage density. Especially for all-organic structure design, enhancing energy storage density is always accompanied by the reduction of mechanical strength, because the previous designs only individually increase energy gap and reduce interchain interaction of polymer structure. Therefore, many literatures only provide the data of enhanced breakdown strength/energy storage density and the corresponding mechanical strength can not be found. Finally, we only counted the literatures with the mechanical strength data, so the corresponding literature quantity in dielectric energy storage filed is relatively small up to now.

In addition, in polymer film, when the thickness decreases to a certain value, the surface morphology and stress distribution will undergo significant changes, so the mechanical property is also decided by polymer film thickness. However, in dielectric energy storage field, it requires the relatively low thickness of polymer film, so almost all literatures prepare the polymer films with similar thickness of 5-10μm, and the lower thickness is difficult to achieve in a large area of polymer film up to now.

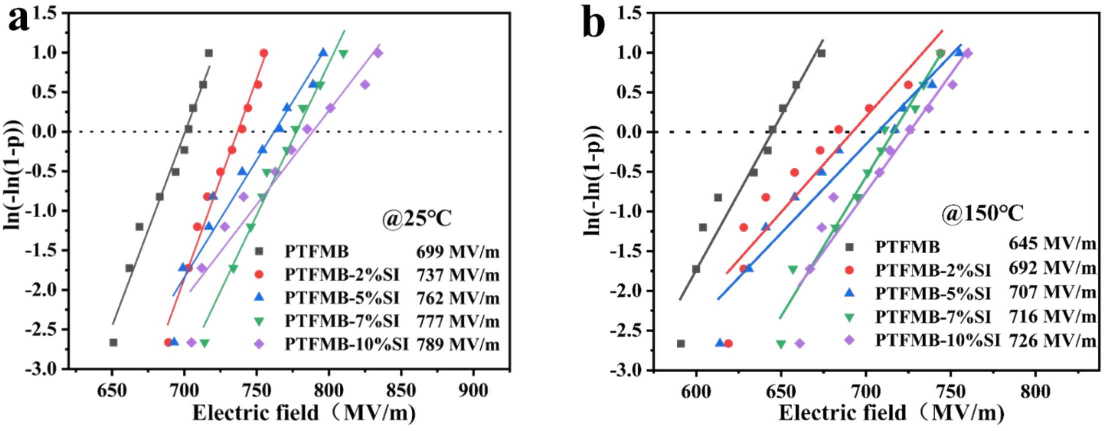

Figure S13. Weibull plots of the breakdown strength for different siloxane modified PTFMB films at (a) 25℃, (b) 150℃.

Table S4. Breakdown strengths and β of PABI, PTFMB and different siloxane modified PTFMB films at 25°C and 150°C.

Sample	25°C		150°C	
	E_b (MV/m)	β	E_b (MV/m)	β
PABI	432	10.2	395	6.4
PTFMB	699	34.1	645	25.1
PTFMB-2%SI	737	37.2	692	16.6
PTFMB-5%SI	762	22.6	707	15.8
PTFMB-7%SI	777	29.9	716	25.2
PTFMB-10%SI	789	18.8	726	21.6

The original breakdown data and Weibull breakdown strength processed for siloxane modified PTFMB at different temperatures are illustrated. It is evident that the breakdown strength of the siloxane modified PTFMB shows a gradual increase with increasing siloxane content. At 25°C, PTFMB-10%SI exhibits the highest breakdown strength of 789 MV/m, representing a 12.9% increase compared to PTFMB. At the elevated temperature of 150°C, due to increased likelihood of thermal breakdown in the materials, the breakdown strengths of the samples decrease to varying extents. However, PTFMB-10%SI still maintains the highest breakdown strength value at 726 MV/m.

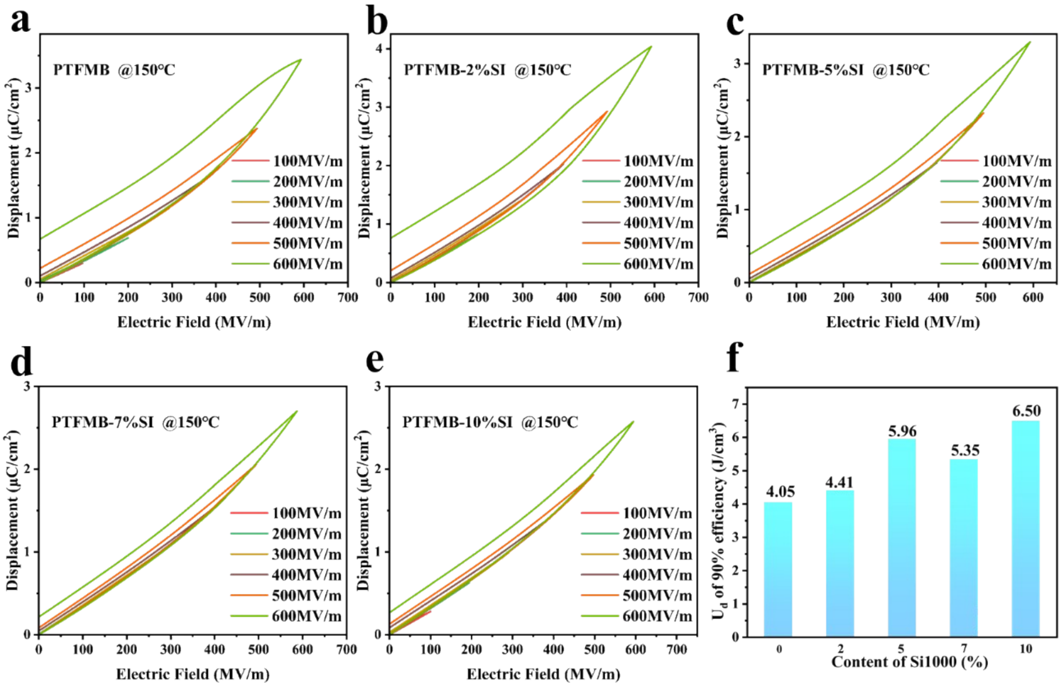

Figure S14. (a-e) *D*-*E* curves of siloxane modified PTFMB films at 150°C. (f) U_d at 90% efficiency measured at 150°C for siloxane modified PTFMB films.

Compared to the pristine PTFMB film, PTFMB-SI films exhibit the narrower D-E loops at the same electric field strength, indicating higher energy storage efficiency. Consequently, when the efficiency (η) exceeds 90% and the temperature is 150°C, the maximum discharge energy density of PTFMB-10%SI film reaches 6.50 J/cm³, representing a 60% improvement over the 4.05 J/cm³ of PTFMB at the same temperature. The excellent high-temperature energy storage performance of PTFMB-10%SI film demonstrates its potential for the use as a capacitor film at elevated temperatures.

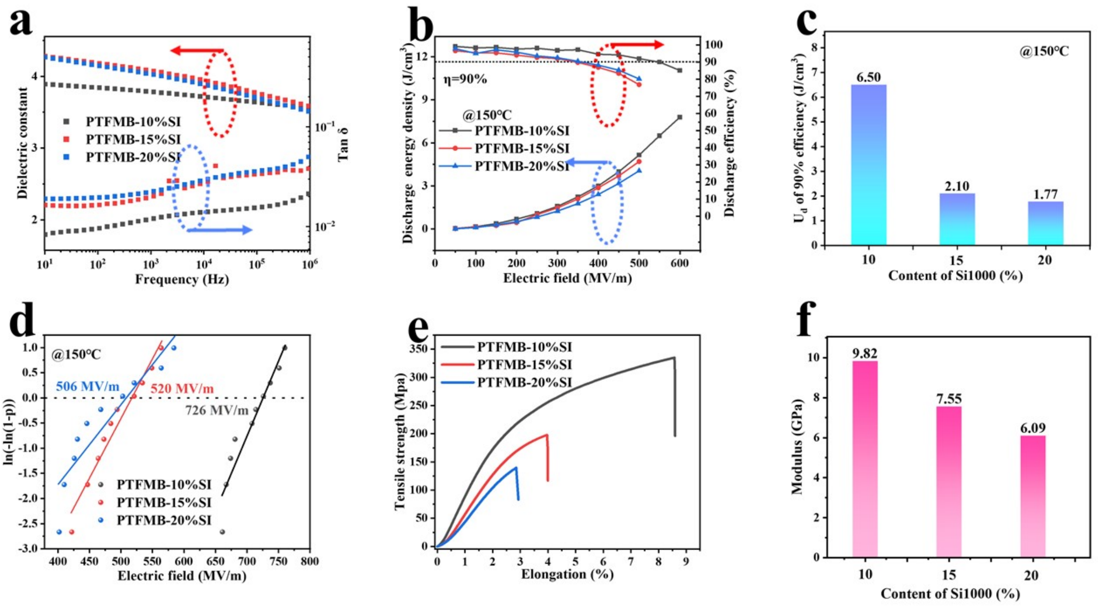

Figure S15. Systematic performance evaluations of PTFMB-15%SI and PTFMB-20%SI films of (a) Dielectric constant and loss (tanδ) at different frequencies. (b) Discharged energy density/efficiency as a function of electric field. (c) Discharged energy density at the 90% efficiency. (d) Weibull distributions of breakdown strength at 150°C. (e) Stress-strain curves. (f) Young's modulus.

Initial observations indicated that SI1000 content beyond 15% led to opaque, wrinkled, and brittle films, and subsequent performance testing of these samples revealed critical limitations. As demonstrated in Figure S15a, the PTFMB-10%SI film achieves the lowest dielectric loss across a broad frequency range, outperforming films with higher SI1000 loadings (15–20%). This performance degradation at elevated SI1000 concentrations arises from disrupt matrix homogeneity and introduce interfacial voids which increased dielectric loss. Besides, relative to the optimal PTFMB-10%SI films, significant performance degradation was observed, including a 73% decrease in energy density (from 6.50 to 1.77 J/cm³) and a 30% reduction in breakdown strength (from 726 to 506 kV/mm). (Figure S15b-d). The mechanical characterization demonstrated significant embrittlement, evidenced by a 59% decline in tensile strength and a modulus reduction from 9.82 GPa to 6.09 GPa (Figure S15e-f). This performance degradation highlighted the critical balance required between SI1000 loading and matrix processability for high-performance dielectric applications.

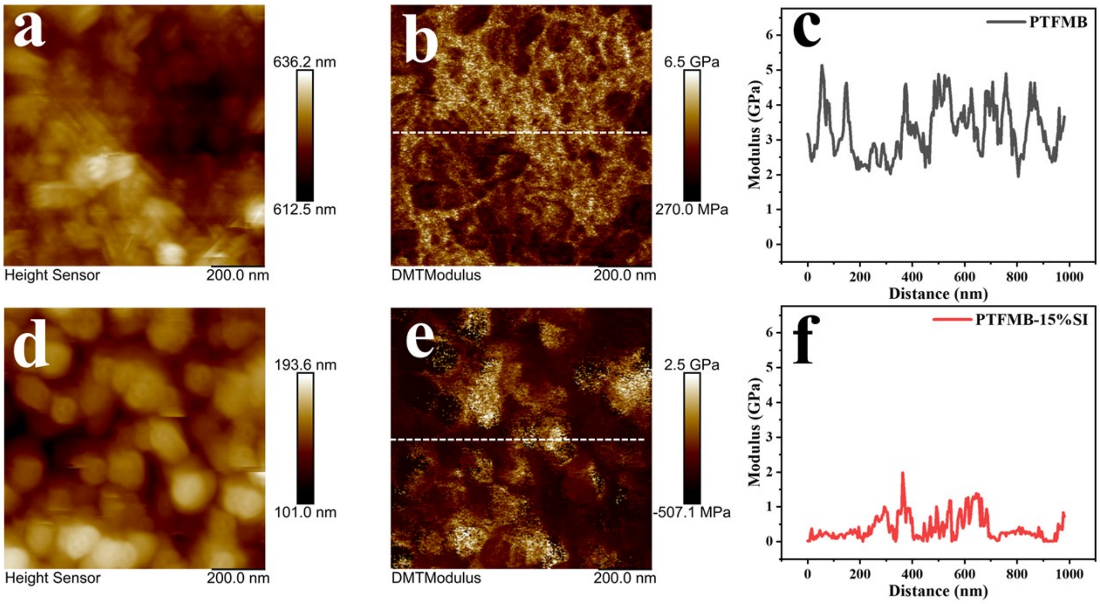

Figure S16. (a) AFM images and (b-c) modulus transition analysis of PTFMB film. (c) AFM images and (d-e) modulus transition analysis of PTFMB-15%SI film.

Atomic force microscopy (AFM) surface topography analysis reveals that pristine PTFMB films exhibit excellent surface smoothness with an average roughness of only 2.1 nm and uniform surface modulus distribution in the range of 2-5 GPa (Figure S16a-c). In contrast, PTFMB-15%SI film demonstrates significantly increased surface roughness (11.7 nm) and reduced surface modulus (0.1-2 GPa), confirming that the incorporation of too high SI1000 components reduce the film quality and influence the surface characteristics and mechanical properties of the films (Figure S16d-e).

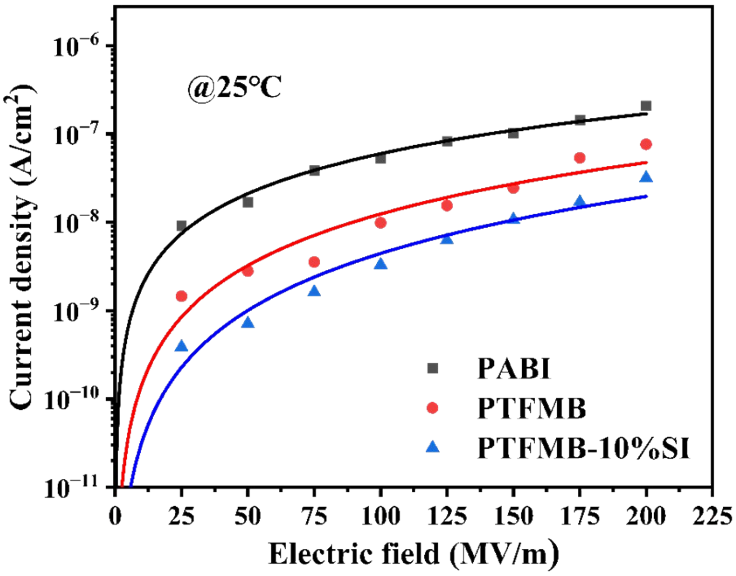

Figure S17. Leakage current density at 25 °C of PABI, PTFMB and PTFMB-10%SI films.

Under the influence of high electric fields, it becomes easier for charges to be injected from the electrodes into the material and for electrons within the material to be excited. Consequently, under high electric field conditions, the leakage current density of dielectrics typically increases significantly, leading to substantial energy loss. At 25°C, PTFMB-10%SI exhibits a lower leakage current density compared to that of PABI and PTFMB at 25-200 MV/m, thus reducing the conduction loss.

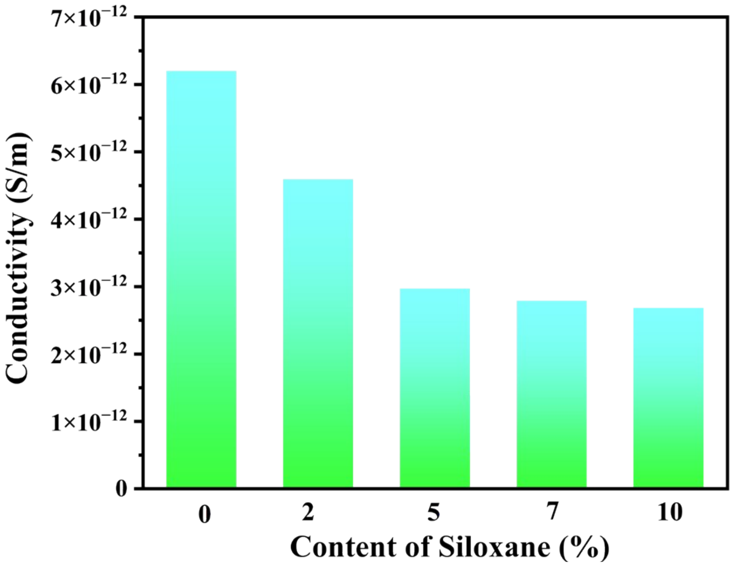

Figure S18. Conductivity of siloxane modified PTFMB films.

The conductivity of pure PTFMB film is the highest, which is 6.2×10^{-12} S/m. With the increase of siloxane content, the conductivity of PTFMB-SI films decreases gradually, and the conductivity of PTFMB-10%SI film decreases to a low level of 2.68×10^{-12} S/m, thus effectively restricting the electron/carrier transport for reducing the conduction loss.

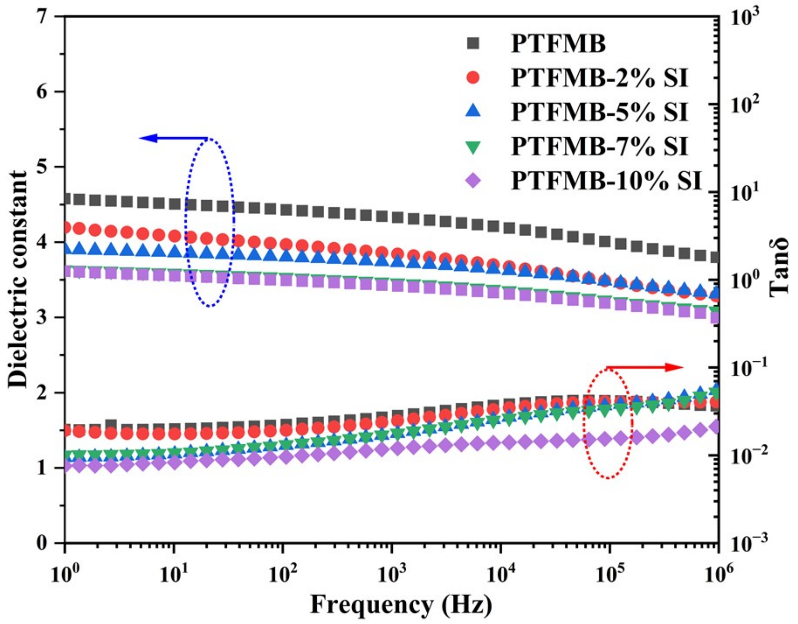

Figure S19. Dielectric constant and loss (tan δ) of siloxane modified PTFMB films.

The dielectric loss of PTFMB-SI film decreases with increased siloxane content. This reduction can be attributed to the inherently low polarity of siloxane unit, resulting in a low polarizability under electric field. Additionally, the introduction of siloxane increases the interchain spacing and free volume, further reducing the polarizability. Meanwhile, siloxane unit also suppresses the conjugation effect of polymer structure. These effects help to lower the dielectric loss of PTFMB-SI film at different frequencies.

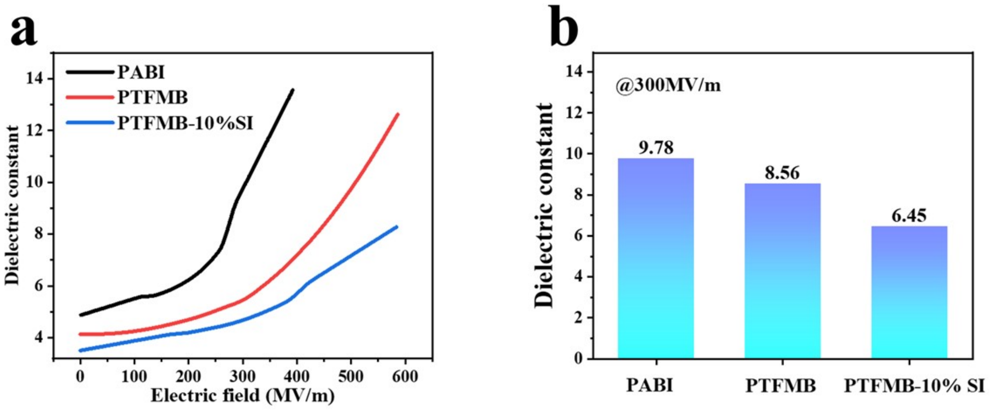

Figure S20. (a) Variation of dielectric constant with electric field for PABI, PTFMB and PTFMB-10%SI films. (b) Dielectric constant of PABI, PTFMB, PTFMB-10%SI film at 300MV/m.

We systematically investigated the dielectric properties of various polymer films under high electric fields (Figure S20). Experimental results demonstrate that PABI films exhibit the highest dielectric constant across all tested electric field intensities, while all three samples show a significant increasing trend in dielectric constant with rising electric field strength, revealing the enhanced polarization effect of polymeric materials under high electric fields.

Table S5. Comparisons of discharged energy density at 150 °C with efficiency above 90%, T_g, ε_r, E_b at 150°C and Young's Modulus between this work and other reported high-temperature dielectric polymers.

Sample	U_d @η=90% (J/cm^3)	T_g (°C)	Young's Modulus (GPa)	ε_r	E_b @150°C (MV/m)
This work	6.50	274	9.8	3.9	726
PEI[1]	1.17	220	2.8	3.2	458
PEEK[2]	0.64	150	3.6	3.1	361
PI-NH_2-POSS[1]	5.24	216	1.8	3.0	610
PI-oxo-iso[4]	6.30	258	2.1	3.1	635
PEI-p[4]	3.1	232	2.3	3.3	561
PEI-o-M[4]	5.1	238	3.9	3.4	581
PI-spiro-1-5[5]	6.12	258	2.9	3.2	674
PI-spiro-2-5[5]	7.29	256	2.9	3.1	694

Notably, the test methods such as electrode area and film thickness may have obvious effects on breakdown strength and thus energy density. However, in dielectric energy storage field, it requires the relatively low thickness of polymer film, so almost all literatures prepare the polymer films with similar thickness of 5-10μm, and the lower thickness is difficult to achieve in a large area of polymer film up to now. Meanwhile, our work and reported literatures adopted the standard metal spraying mould, so the electrode area should have similar value with diameter of about 5 mm.

In addition, electro-mechanical breakdown can be observed in polymers which is related to the deformation of dielectrics under Maxwell stress[6,7]. According to the Stark-Garton model, the electro-mechanical breakdown strength is positively correlated with the Young's modulus[8].

$$E_b = 0.606\left(\frac{Y}{\varepsilon_0\varepsilon_r}\right)^{0.5} \# \quad 1.$$

Therefore, a high Young's modulus in polymer dielectrics can effectively prevent electro-mechanical breakdown, thereby enhancing their breakdown strength. However, the currently reported polymer dielectrics in dielectric energy storage field exists an intractable and contradictory problem that synergistically enhancing the modulus and breakdown strength/energy storage density. Especially for all-organic structure design, enhancing breakdown strength and energy storage density/efficiency is always accompanied by the reduction of modulus, because previous designs always individually increase energy gap and reduce interchain interaction of polymer structure. Therefore, many literatures only provide the data of enhanced breakdown strength/energy storage density and the corresponding modulus can not be found. Finally, we only counted the literatures with both breakdown strength/energy storage density and the mechanical strength data, so the corresponding literature quantity in dielectric energy storage filed is relatively small up to now.

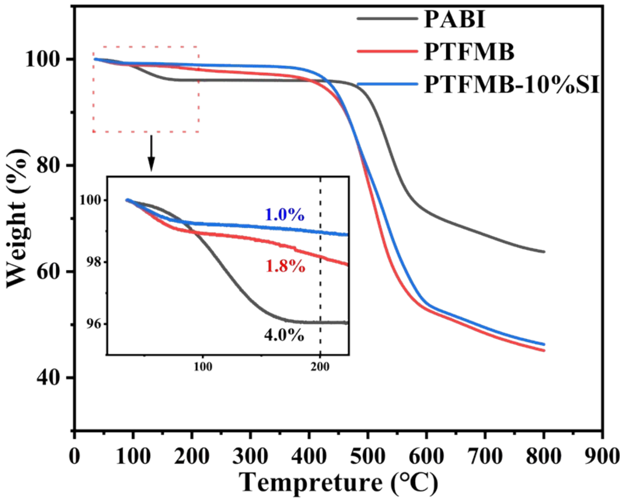

Figure S21. TGA curves of PABI, PTFMB and PTFMB-10%SI films.

From the TGA curves, it can be observed that both PTFMB and PTFMB-SI exhibit no significant weight loss between 40°C and 400°C. The weight loss in this temperature range is primarily due to moisture. During 40°C to 400°C, PTFMB-SI films show even less weight loss, indicating a lower water absorption rate compared to PTFMB and PABI films.

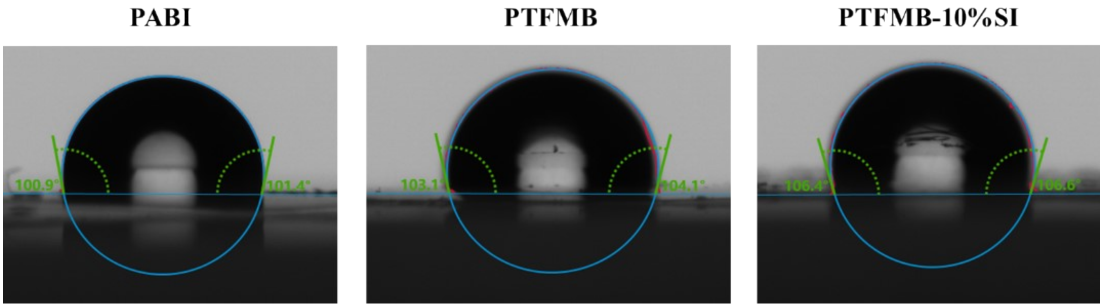

Figure S22. Water contact angle test photos of PABI, PTFMB and PTFMB-10%SI films.

The water contact angle test photos show the water contact angle gradually increases from PABI film to PTFMB-10%SI film, which also reflects the enhanced moisture-resistant ability.

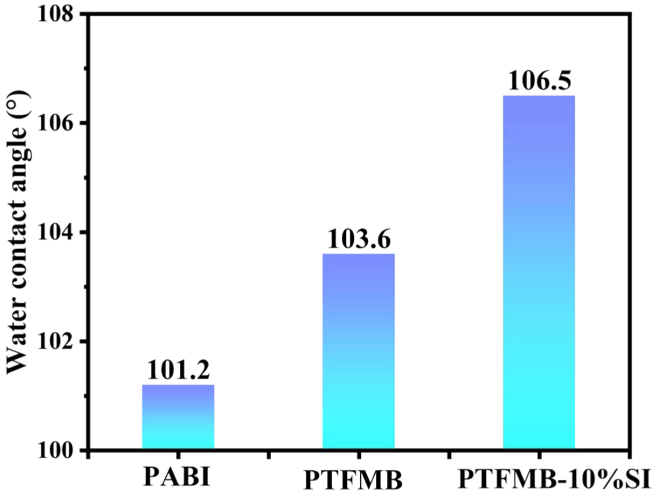

Figure S23. Water contact angle of PABI, PTFMB and PTFMB-10%SI films.

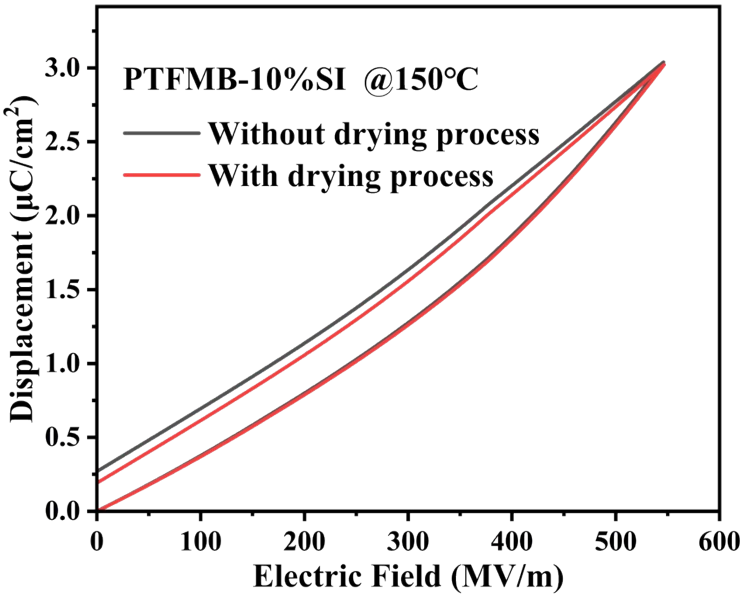

Figure S24. D-E curves of PTFMB-10%SI films without and with drying process.

There is little change in the energy storage efficiency of PTFMB-10%SI film before and after drying treatment, attributed to its good moisture-resistant ability.

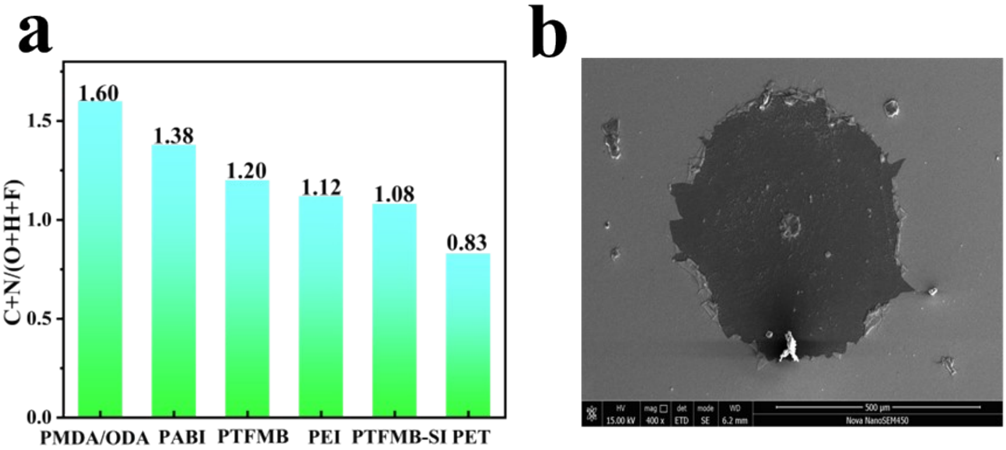

Figure S25. (a) Ratio of (C+N) to (H+O+F) of different polymers. (b) SEM image of PTFMB-10%SI film after electrical breakdown.

It is empirically understood that a low ratio of (C+N) to (H+O+F) typically provides polymer dielectrics with self-healing ability. For PTFMB-10%SI, the ratio is 1.08, much lower than Kapton PI (1.60) and PABI (1.38). It is evident that electrical breakdown has caused extensive vaporization of the metal electrodes, exposing the underlying insulating dielectric. Consequently, around the breakdown holes, there is a substantial insulating region between the carbonized conductive area and the surrounding metal electrode. This lack of an effective conductive pathway ensures overall insulation performance.

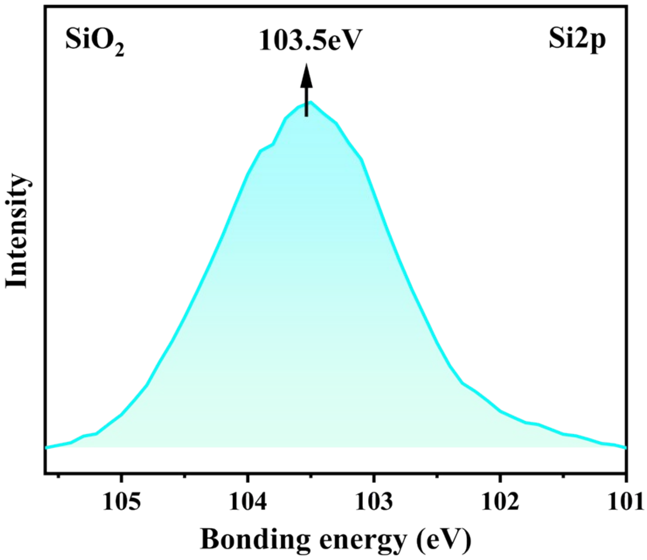

Figure S26. Si2p XPS spectra with fitting curves of SiO$_2$.

The peak position of SiO$_2$ in its Si2p XPS spectra is at 103.5 eV (Figure S26), and the peak position of siloxane unit in the Si2p XPS spectra of PTFMB-SI is at 101.6 eV. After partial discharge etching, the Si2p XPS spectra of PTFMB-SI produce two peaks, and the peak position at 103.5 eV is leading, which indicates that the introduced siloxane unit in PTFMB-SI in situ transforms into SiO$_2$-like structure during partial discharge etching.

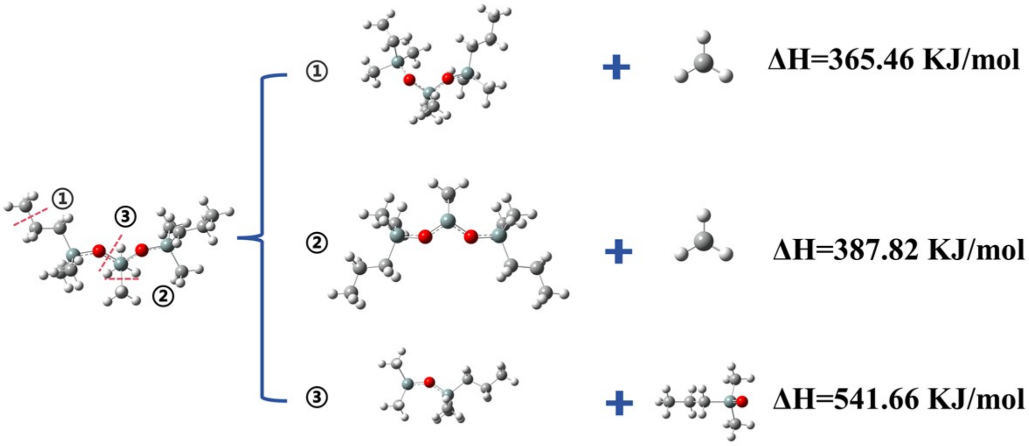

Figure S27. Cleavage products and corresponding bond dissociation energies (BDE) at different sites of siloxane units.

Under corona discharge conditions, organosilicon compounds transform into SiO_2-like structures will undergo selective bond cleavage, with three primary dissociation pathways identified: (1) C–C bond rupture, (2) Si–C bond scission, and (3) Si–O bond breakage. Computational simulations reveal distinct bond dissociation energies (BDEs) for these critical bonds: 365.46 kJ/mol for C–C, 387.82 kJ/mol for Si–C, and 541.66 kJ/mol for Si–O. The significantly higher BDE of the Si–O bond demonstrates its superior thermodynamic stability compared to organic moieties (C–C and Si–C bonds). Consequently, corona discharge process preferentially targets the siloxane units through lower-energy cleavage pathways before affecting the more robust Si–O linkages. The gradual cleavage of C–C and Si-C bonds, and the reservation of Si–O bond result in the transformation from siloxane units to SiO_2-like structures.

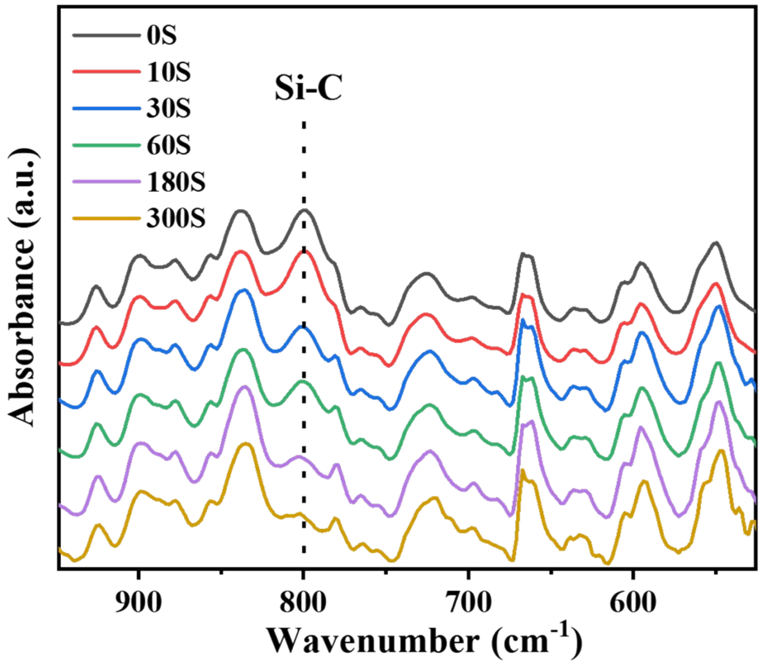

Figure S28. ATR-FTIR spectra of PTFMB-10%SI films for various corona discharge aging times.

Fourier-transform infrared (FTIR) spectroscopy analysis revealed a significant intensity reduction of the characteristic Si-C bond absorption peak at 801 cm^{-1} with prolonged corona discharge time. This observation clearly demonstrates the progressive decomposition and removal of organic components (e.g., Si-CH_3) in the organosilicon material during corona discharge.

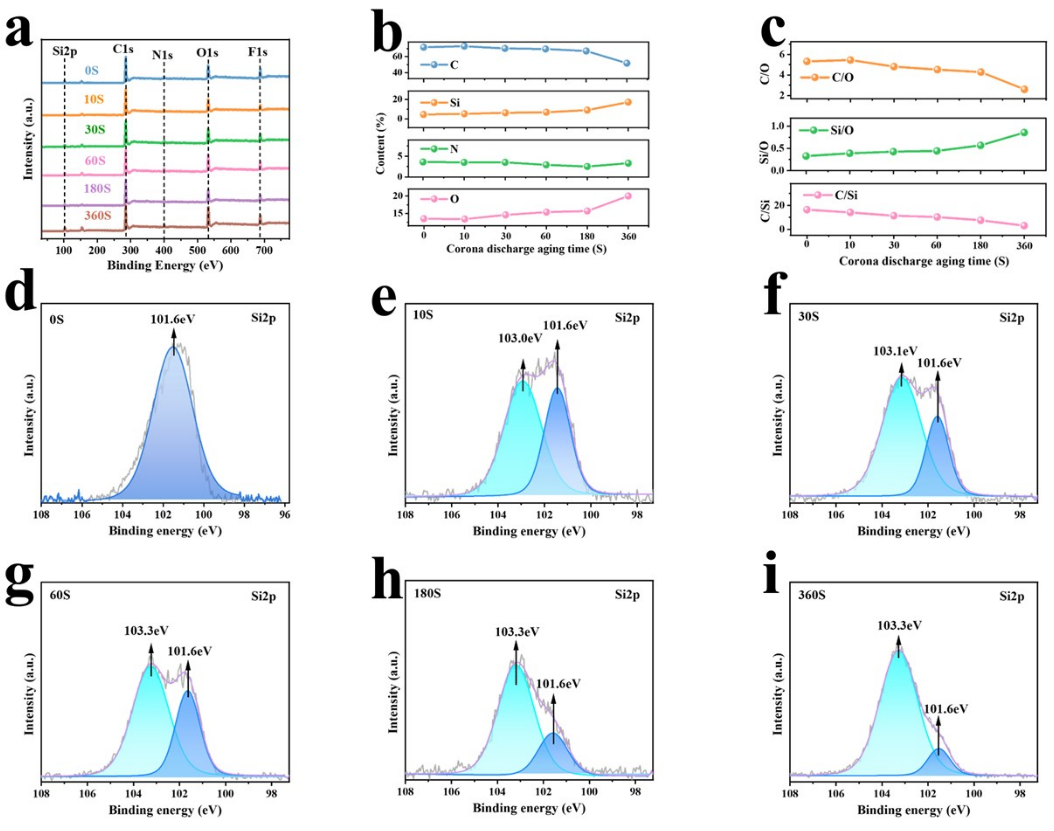

Figure S29. (a) XPS spectra of PTFMB-10%SI films for various corona discharge aging time. (b) The content of different chemical elements of PTFMB-10%SI films for various corona discharge aging time. (c) C/O, Si/O and Si/C ratios of PTFMB-10%SI films for various corona discharge aging time. (d-e) Si2p XPS spectra with fitting curves of PTFMB-10%SI films for various corona discharge aging time.

X-ray photoelectron spectroscopy (XPS) analysis of PTFMB-10%SI film before and after corona discharge revealed the presence of C, N, O, F, and Si elements (Figure S29a). Prolonged corona discharge duration led to a continuous decrease in atomic percentage of C, indicating progressive removal of organic components, while concurrent increases in Si and O content confirmed the enrichment of Si-O structures (Figure S29b). The decreased C/Si ratio further supported preferential etching of carbon species bonded to silicon (Figure S29c). Deconvolution of Si 2p spectra showed the untreated sample exhibited a peak at 101.6 eV (attributed to SI1000), whereas a new peak emerged at 103.0 eV (assigned to SiO_2) after 10-second etching (Figure S29d-i). This SiO_2 peak area expanded with extended etching time, accompanied by diminishing SI1000 peak intensity. Quantitative analysis demonstrated approximately 88.73% conversion of SI1000 to SiO_2 after 300-second corona treatment, elucidating the discharge-induced transformation from organosilicon to SiO_2-like structure (Figure S30).

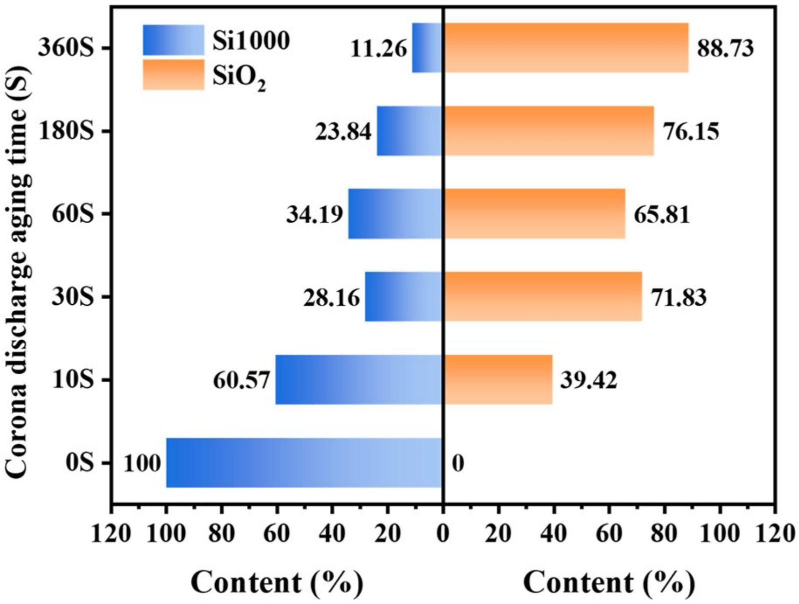

Figure S30. Contents of SiO_2 and siloxane unit of PTFMB-10%SI films for various corona discharge aging time.

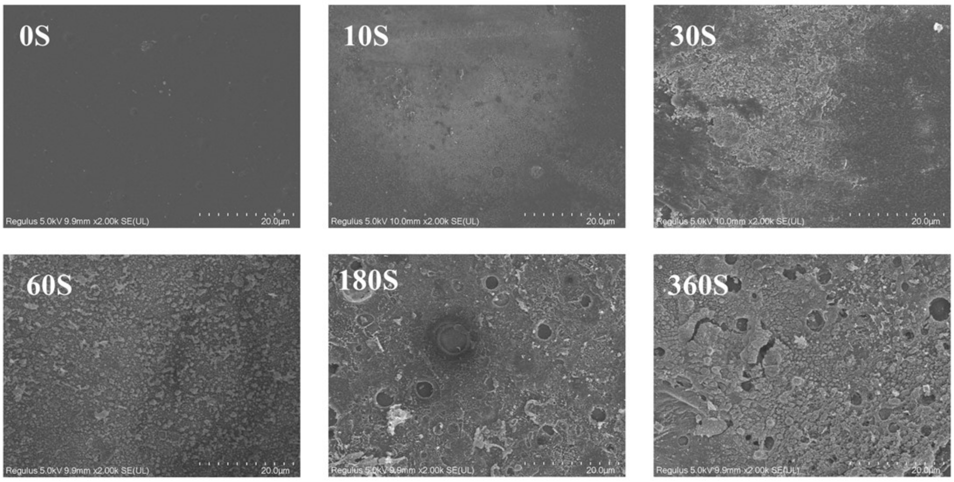

Figure S31. SEM photos of PTFMB-10%SI films for various corona discharge aging time.

In addition, the surface morphological evolution of PTFMB-10%SI films under corona discharge was systematically investigated. Key findings reveal a strong time-dependent degradation pattern: Short-term corona discharge (≤60s) induced dispersed nanoparticles, presumably residual SiO_2-like structures after organic component removal. Extended corona discharge (180-360s) generated distinct porous structures, demonstrating that even the SiO_2-like frameworks eventually succumbed to prolonged corona discharge, evidencing the multi-level destructive effects of corona discharge on the material.

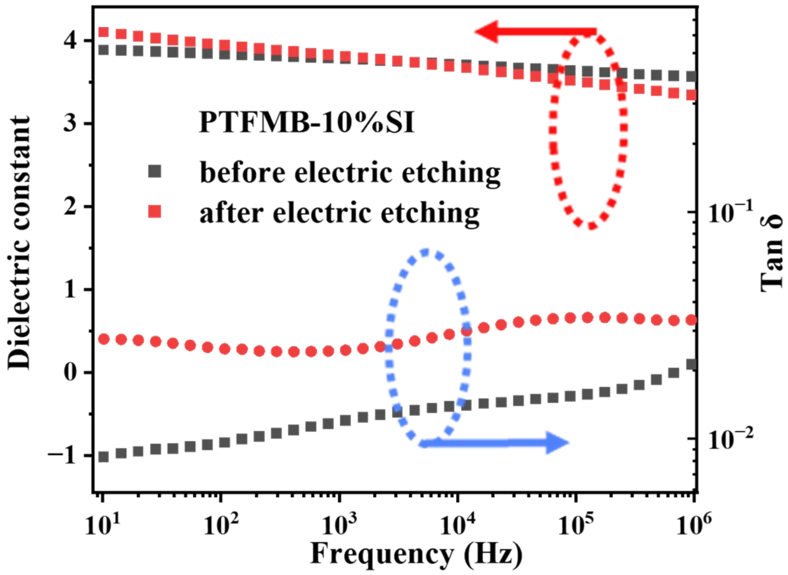

Figure S32. Performance evaluations of PTFMB-10%SI film before and after electric etching: Dielectric constant and loss (tanδ) at different frequencies.

Specifically, after electric etching, the PTFMB-10%SI film exhibits an increased dielectric constant in the low-frequency region compared to the pristine sample. Across the entire frequency range, a significant rise in dielectric loss is observed, resulting from molecular chain degradation and defect formation induced by the etching process.

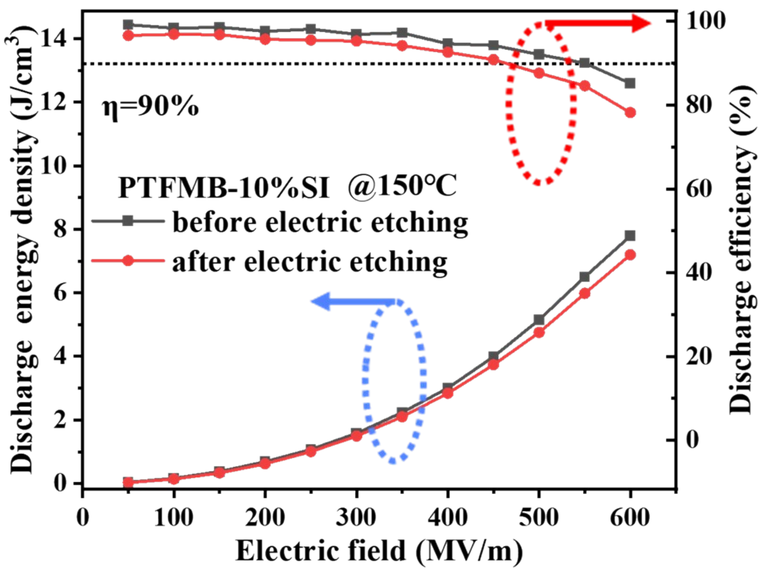

Figure S33. Performance evaluations of PTFMB-10%SI film before and after electric etching: Discharged energy density/efficiency as a function of electric field.

Further energy storage testing demonstrates that molecular chain degradation contributes to elevated energy loss, consequently decreasing both storage efficiency and energy density, but the corresponding decreased degree is very small.

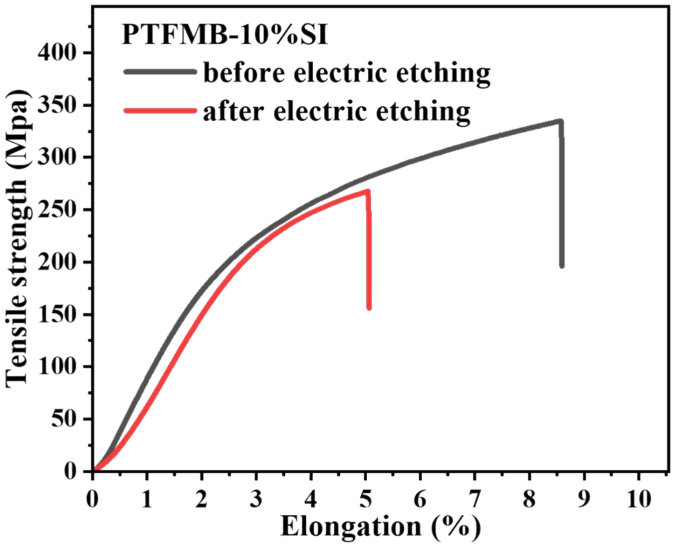

Figure S34. Performance evaluations of PTFMB-10%SI film before and after electric etching: Stress-strain curves.

Besides, mechanical characterization reveals that the modulus remains largely unchanged before and after electric etching, indicating the bulk structure remains intact. However, surface defects lead to reduced tensile strength and elongation.

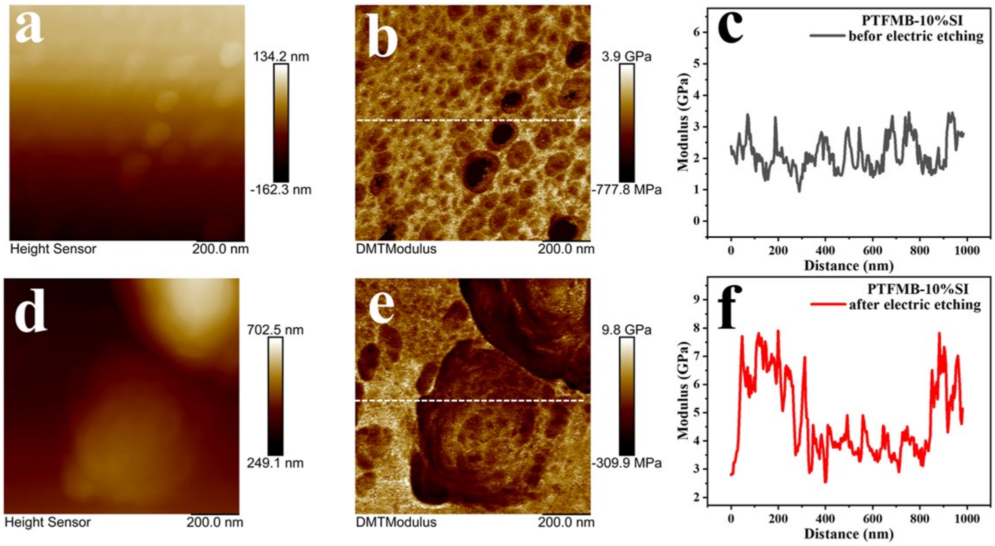

Figure S35. (a) AFM images and (b-c) surface modulus analysis of PTFMB-10%SI film before electric etching. (c) AFM images and (d-e) surface modulus analysis of PTFMB-10%SI film after electric etching.

AFM characterization reveals significant surface modifications after corona treatment: the average roughness dramatically increases from 6.56 nm to 45.3 nm, indicating surface damage caused by corona discharge etching, which is consistent with SEM observations. Remarkably, the surface modulus distribution shows substantial changes - while the pre-treatment modulus uniformly ranges between 1-4 GPa, post-treatment local regions exhibit high modulus characteristics (4-9 GPa). These high-modulus regions confirm the formation of inorganic SiO_2-like structures on the surface after selective removal of organic components during corona discharge etching.

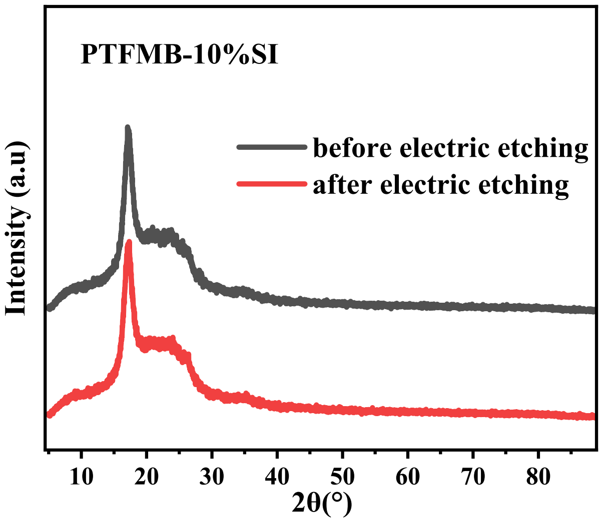

Figure S36. XRD curves of PTFMB-10%SI film before and after electric etching.

X-ray diffraction (XRD) analysis shows no significant changes in diffraction patterns before and after corona discharge etching. This observation can be attributed to two factors: (1) the corona-induced inorganic components may only exist in an ultra-thin surface layer below the XRD detection limit, and (2) the formed SiO_2-like structures likely remain in an amorphous state without developing long-range crystalline order.

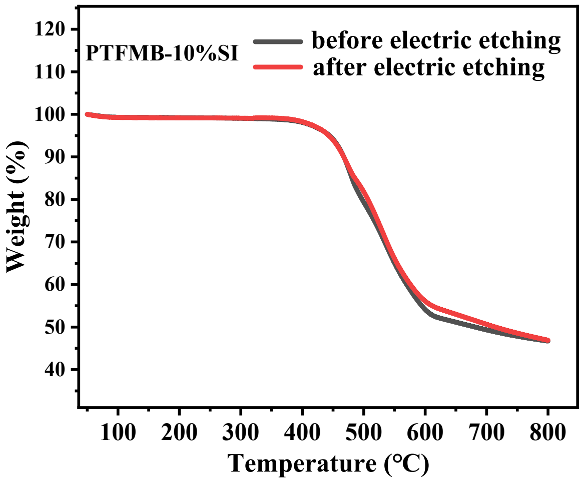

Figure S37. TGA curves of PTFMB-10%SI film before and after electric etching.

TGA results demonstrate that corona treatment does not compromise the overall thermal stability of the film. The residual mass percentage at high temperatures (400-600℃) remains consistent with untreated samples, and the primary decomposition stage shows no significant shift. These findings indicate that while corona discharge etching induces localized surface modifications (e.g., inorganic SiO_2-like structures formation), it does not substantially alter the bulk thermal degradation behavior or heat resistance of the film.

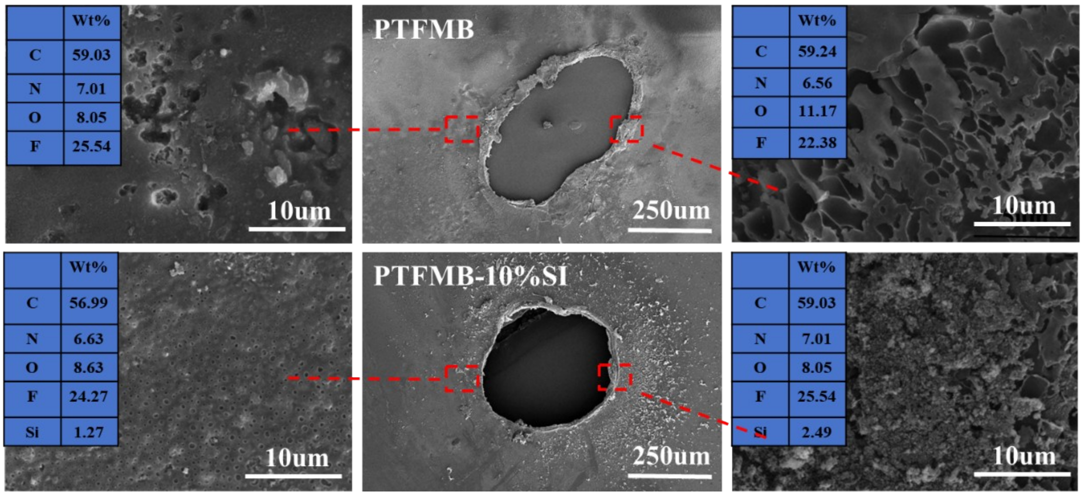

	Wt%
C	59.03
N	7.01
O	8.05
F	25.54

	Wt%
C	59.24
N	6.56
O	11.17
F	22.38

	Wt%
C	56.99
N	6.63
O	8.63
F	24.27
Si	1.27

	Wt%
C	59.03
N	7.01
O	8.05
F	25.54
Si	2.49

Figure S38. SEM images and element contents of PTFMB and PTFMB-10%SI films after partial discharge breakdown.

It can be observed that after partial discharge breakdown, the edge regions of breakdown holes in PTFMB film contain numerous voids, indicating severe polymer damage at those sites. In contrast, PTFMB-10%SI film shows a significant presence of uniformly distributed SiO_2-like particles at the edges of breakdown perforations, effectively inhibiting electrical etching and demonstrating stronger resistance to partial discharge etching.

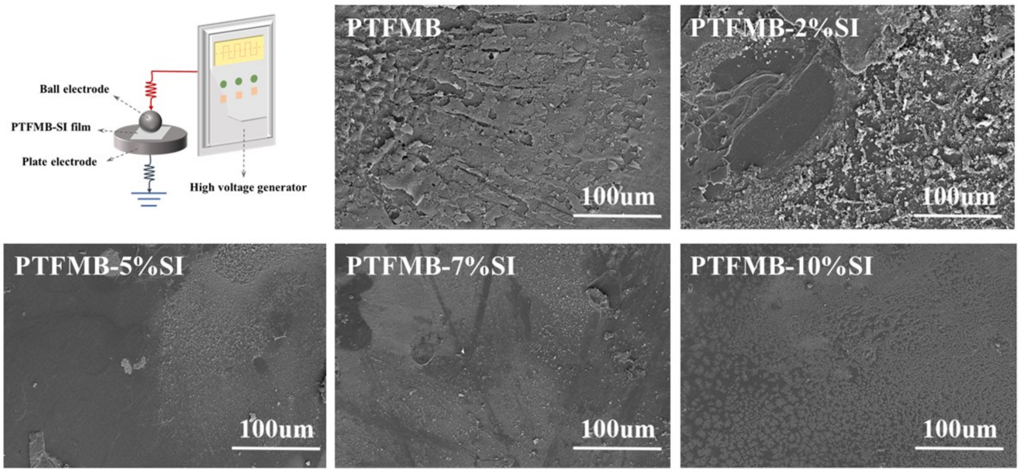

Figure S39. Schematic of partial discharge test and SEM images of siloxane modified PTFMB films after partial discharge etching at the same time.

The results indicate that with the same partial discharge etching time, the degree of surface damage on the films decreases as the siloxane content increases. The surface of the pristine PTFMB film, after partial discharge etching, exhibits numerous holes and polymer debris, indicating severe damage from the partial discharge. In contrast, the surface of the PTFMB-SI films especially PTFMB-10%SI film forms numerous densely packed SiO_2-like particles, providing effective protection to resist partial discharge etching.

References

1 J. Dong, L. Li, P. Qiu, Y. Pan, Y. Niu, L. Sun, Z. Pan, Y. Liu, L. Tan, X. Xu, C. Xu, G. Luo, Q. Wang and H. Wang, *Adv. Mater.*, 2023, **35**, 2211487.
2 H. Li, L. Ren, Y. Zhou, B. Yao and Q. Wang, *High Voltage*, 2020, **5**, 365–376.
3 M. Yang, S. Wang, J. Fu, Y. Zhu, J. Liang, S. Cheng, S. Hu, J. Hu, J. He and Q. Li, *Adv. Mater.*, 2023, **35**, 2301936.
4 R. Wang, Y. Zhu, J. Fu, M. Yang, Z. Ran, J. Li, M. Li, J. Hu, J. He and Q. Li, *Nat. Commun.*, 2023, **14**, 2406.
5 Z. Ran, R. Wang, J. Fu, M. Yang, M. Li, J. Hu, J. He and Q. Li, *Adv. Mater.*, 2023, **35**, 2303849.
6 Y. Zhu, Z. Shen, Y. Li, B. Chai, J. Chen, P. Jiang and X. Huang, *Nano Micro Lett.*, 2022, **14**, 151.
7 J. Chen-Roetling and R. F. Regan, *J. Neurochem.*, 2016, **139**, 586–595.
8 K. H. Stark and C. G. Garton, *Nature*, 1955, **176**, 1225–1226.